J Biomol NMR (2009) 45:185–196
DOI 10.1007/s10858-009-9352-9

ARTICLE

# Effects of amantadine on the dynamics of membrane-bound influenza A M2 transmembrane peptide studied by NMR relaxation

**Sarah D. Cady · Mei Hong**

Received: 8 May 2009 / Accepted: 26 June 2009 / Published online: 25 July 2009


**Abstract** The molecular motions of membrane proteins in liquid-crystalline lipid bilayers lie at the interface between motions in isotropic liquids and in solids. Specifically, membrane proteins can undergo whole-body uniaxial diffusion on the microsecond time scale. In this work, we investigate the $^{1}$H rotating-frame spin-lattice relaxation ($T_{1\rho}$) caused by the uniaxial diffusion of the influenza A M2 transmembrane peptide (M2TMP), which forms a tetrameric proton channel in lipid bilayers. This uniaxial diffusion was proved before by $^{2}$H, $^{15}$N and $^{13}$C NMR lineshapes of M2TMP in DLPC bilayers. When bound to an inhibitor, amantadine, the protein exhibits significantly narrower linewidths at physiological temperature. We now investigate the origin of this line narrowing through temperature-dependent $^{1}$H $T_{1\rho}$ relaxation times in the absence and presence of amantadine. Analysis of the temperature dependence indicates that amantadine decreases the correlation time of motion from 2.8 ± 0.9 μs for the apo peptide to 0.89 ± 0.41 μs for the bound peptide at 313 K. Thus the line narrowing of the bound peptide is due to better avoidance of the NMR time scale and suppression of intermediate time scale broadening. The faster diffusion of the bound peptide is due to the higher attempt rate of motion, suggesting that amantadine creates better-packed and more cohesive helical bundles. Analysis of the temperature dependence of $\ln\left(T_{1\rho}^{-1}\right)$ indicates that the activation energy of motion increased from 14.0 ± 4.0 kJ/mol for the apo peptide to 23.3 ± 6.2 kJ/mol for the bound peptide. This higher activation energy indicates that excess amantadine outside the protein channel in the lipid bilayer increases the membrane viscosity. Thus, the protein-bound amantadine speeds up the diffusion of the helical bundles while the excess amantadine in the bilayer increases the membrane viscosity.

**Electronic supplementary material** The online version of this article (doi:10.1007/s10858-009-9352-9) contains supplementary material, which is available to authorized users.

S. D. Cady · M. Hong (✉)
Department of Chemistry, Iowa State University, Ames, IA 50011, USA
e-mail: mhong@iastate.edu

## Introduction

Nuclear magnetic resonance has long been used as a tool for measuring molecular dynamics over a broad range of time scales, from the fast picosecond–nanosecond regime (Mandel et al. 1996), to the slow microsecond–millisecond regime (Palmer et al. 2001; Schaefer et al. 1977; Shaw et al. 2000), and to the ultra-slow supra-second regime (deAzevedo et al. 2000; Schmidt et al. 1988). Some of the most interesting applications are to biomolecules, where molecular dynamics has a particularly strong connection to function (Ishima and Torchia 2000; Kay 1998; Palmer et al. 1996). In solution NMR studies of biomolecular dynamics, $^{15}$N relaxation NMR has been the method of choice and the Lipari–Szabo model-free formalism (Clore et al. 1990; Lipari and Szabo 1982) has provided a simple theoretical framework to separate the effects of internal anisotropic motions from whole-body isotropic motion and to extract the amplitudes and rates of internal motion.

In the solid state, the lack of isotropic molecular tumbling considerably simplifies studies of internal motions by NMR. Many solid-state NMR techniques directly probe the amplitudes of internal motions, most notably $^{2}$H quadrupolar NMR (Jelinski et al. 1980), which has exquisite angular resolution but no chemical resolution, and $^{1}$H–X dipolar coupling techniques under magic-angle spinning

(MAS), which have chemical site resolution (Hong et al. 2002; Munowitz et al. 1982; Schaefer et al. 1983). Nuclear spin relaxation times ($T_1$, $T_2$ and $T_{1\rho}$) have also been used to determine the correlation times and activation energies of motional processes such as methyl three-site jumps and aromatic ring flips. Combined, these amplitude and rate measurements have provided detailed information on the dynamics of structural proteins such as collagen and silk (Jelinski et al. 1980; Yang et al. 2000), enzymes (Williams and McDermott 1995), and lipid membranes (Blume et al. 1982; Smith and Oldfield 1984). Molecular motions of synthetic polymers (Hagemeyer et al. 1989; Schaefer et al. 1990; Schaefer et al. 1984) and small molecules (Rothwell and Waugh 1981) have also been investigated extensively using solid-state NMR.

The dynamic environment of liquid-crystalline lipid bilayers lies at the interface between isotropic fluids and rigid solids and hence presents unique challenges to understanding membrane protein dynamics. While membrane protein sidechain motions have been studied by NMR for decades (Huster et al. 2001; Kinsey et al. 1981; Lee et al. 1993; Opella 1986), whole-body uniaxial rotational diffusion of membrane proteins has been less examined by NMR. As the symmetry axis of the lipid bilayer, the bilayer normal is the axis around which phospholipids undergo nanosecond rotational diffusion (Bloom et al. 1991; Gennis 1989). Membrane proteins can also undergo such rotational diffusion, because the same principle that underlies the phospholipid motion, which is Brownian diffusion in a two-dimensional fluid (Saffman and Delbruck 1975), also applies to membrane proteins. A number of examples of this uniaxial diffusion have now been reported for membrane peptides and proteins (Hong 2007; Hong and Doherty 2006; Lewis et al. 1985; Macdonald and Seelig 1988; Pauls et al. 1985; Prosser et al. 1992; Tian et al. 1998; Yamaguchi et al. 2001). Their NMR fingerprints include powder lineshapes with reduced anisotropy and an asymmetry parameter ($\eta$) of 0, vanishing intensity at the isotropic chemical shift of non-spinning cross polarization (CP) spectra, and narrow lines in macroscopically aligned samples whose alignment axis deviates from the static magnetic field (Aisenbrey and Bechinger 2004; Glaser et al. 2004; Park et al. 2006).

The influenza A M2 protein forms a proton channel in the virus envelope that is important for the virus life cycle (Pinto et al. 1992; Pinto and Lamb 2007). Acidification of the virus interior uncoats the viral RNA and releases it into the host cell. Amantadine binds the M2 proton channel and prevents its opening, thus inhibiting viral replication (Hay et al. 1985; Wang et al. 1993). The protein forms a tetrameric helical bundle in the membranes of both whole cells (Sakaguchi et al. 1997) and synthetic lipids (Luo and Hong 2006). It undergoes uniaxial diffusion at a rate of $\sim 10^5$/s in DLPC bilayers based on $^2$H NMR spectra and the 2D Brownian diffusion theory (Cady et al. 2007; Kovacs and Cross 1997). The motional axis is the bilayer normal, which is also the helical bundle axis. Since the TM helices have tilt angles of $\sim 38°$ in DLPC bilayers (Cady and Hong 2008), the rotational diffusion has large amplitudes. Combined with the fact that the motional rate is not orders of magnitude different from the $^1$H–$^{13}$C and $^1$H–$^{15}$N dipolar couplings, the motion strongly impacts the NMR spectra: the ambient-temperature $^1$H-decoupled $^{13}$C and $^{15}$N spectra of the protein in lipid bilayers are severely exchange-broadened under both MAS and static conditions (Cady et al. 2007; Li et al. 2007). Interestingly, upon amantadine binding, the resonances in both MAS and static solid-state NMR spectra of the protein sharpen considerably. This line narrowing was also observed in solution NMR spectra of M2 (18–60) bound to DHPC micelles when an excess of the analogous rimantadine was added (Schnell and Chou 2008).

Previously we have compared the $^1$H-decoupled $^{13}$C $T_2$ relaxation times of the apo and bound M2TMP in DLPC bilayers to understand the amantadine-induced line narrowing. We found that the bound peptide has 30–150% longer $^{13}$C $T_2$ than the apo state at 303 K (Cady and Hong 2008; Cady et al. 2009), indicating that the line narrowing has a significant contribution from dynamic changes of the protein. However, the nature of this amantadine-induced relaxation time increase has not been elucidated.

In this work, we have measured and analyzed temperature-dependent $^1$H $T_{1\rho}$ relaxation times of the apo and amantadine-bound M2TMP to better understand its motional properties. We quantify the rates and activation energies of the M2TMP microsecond motion in the absence and presence of amantadine. We find that amantadine increases the motional rates approximately threefold at 313 K by increasing the attempt rates, thus alleviating intermediate time scale broadening and narrowing the spectral lines. Further, excess amantadine in the bilayer increases the activation energy of the motion, whose physical origin will be discussed.

## Materials and methods

### Peptides and lipids

FMOC-protected uniformly $^{13}$C, $^{15}$N-labeled amino acids were either prepared in-house (Carpino and Han 1972) or purchased from Sigma–Aldrich and Cambridge Isotope Laboratories. The M2 transmembrane domain (residues 22–46) of the Influenza A Udorn strain (Ito et al. 1991) was synthesized by PrimmBiotech (Cambridge, MA) and purified to >95% purity. The amino acid sequence is

SSDPL VVAASII GILHLIL WILDRL. Three labeled peptides were used in this work, each with three to four uniformly $^{13}C$, $^{15}N$-labeled residues. They are LAGI (L26, A29, G34 and I35), VAIL (V27, A30, I33 and L38), and VSL (V28, S31 and L36).

### Membrane sample preparation

M2TMP was reconstituted into 1,2-dilauroyl-*sn*-glycero-3-phosphatidylcholine (DLPC) bilayers by detergent dialysis (Luo and Hong 2006). The lipid vesicle solution was prepared by suspending dry DLPC powder in 1 ml phosphate buffer (10 mM $Na_2HPO_4/NaH_2PO_4$, 1 mM EDTA, 0.1 mM $NaN_3$) at pH 7.5, vortexing and freeze–thawing six times to create uniform vesicles (Traikia et al. 2000). M2TMP was dissolved in octyl-$\beta$-D-glucopyranoside (OG) in 2 ml phosphate buffer, then mixed with an equal volume of DLPC vesicles, and dialyzed against the phosphate buffer at 4°C for 3 days. The final peptide/lipid molar ratio was 1:15. The dialyzed peptide-DLPC solution was centrifuged at 150,000*g* to give a pellet containing ~50 wt% water. For the amantadine-bound samples, 10 mM amantadine hydrochloride was added to the phosphate buffer. After pelleting, the amount of amantadine remaining in the supernatant was quantified by $^1H$ solution NMR, and the bound fraction indicates a peptide:amantadine molar ratio of ~1:8 (Cady et al. 2009). All membrane-bound M2 samples were thus studied at pH 7.5, corresponding to the closed state of the channel.

### Solid-state NMR spectroscopy

NMR experiments were carried out on a Bruker AVANCE-600 (14.1 Tesla) spectrometer (Karlsruhe, Germany) using a 4 mm MAS probe. $^1H$ $T_{1\rho}$ measurements were carried out using a Lee-Goldburg (LG) spin lock sequence shown in Fig. 1 (Huster et al. 2001). The initial two 90° and 35° $^1H$ pulses prepare the $^1H$ magnetization to be alternately parallel and antiparallel to the $^1H$ spin lock axis, which lies at the magic angle $\cos^{-1}(1/\sqrt{3})$ from the static magnetic field in the *yz* plane. The spin-lock effective field strength, $\omega_e$, was fixed at $2\pi \times 61.2$ kHz in all experiments, since $T_{1\rho}$ depends on $\omega_e$ (1–2). The samples were spun at 7,000 Hz during all experiments. Six or seven spin lock time points $\tau_{SL}$ were measured between 0 and 8 ms to obtain the $^1H$ $T_{1\rho}$ at each temperature, and six or seven temperatures were measured per peptide to provide a sufficient number of data points in the $\ln\left(T_{1\rho}^{-1}\right)$ versus inverse temperature plot (Fig. 5) to extract the dynamic parameters. The NMR probe and samples were equilibrated for 30 min at each temperature before tuning and data acquisition. The $^1H$ LG–CP period had the same field strength as the LG spin lock period, but had a constant contact time of 300 μs. Typical radiofrequency (rf) pulse lengths were 5 μs for $^{13}C$ and 3.5–4.0 μs for $^1H$. $^{13}C$ chemical shifts were referenced to the α-Gly $^{13}C'$ signal at 176.49 ppm on the TMS scale.

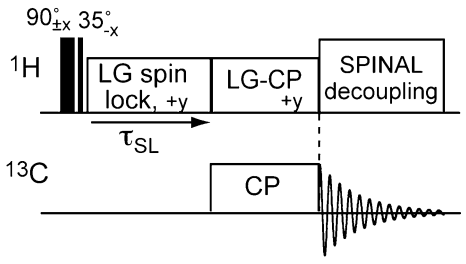


**Fig. 1** $^{13}C$-detected $^1H$ Lee-Goldburg spin lock pulse sequence used to measure $^1H$ $T_{1\rho}$ relaxation times. The $^1H$ magnetization is spin-locked for a variable time $\tau_{SL}$. The LG spin-lock and LG–CP have the same field strength

The $^1H$ $T_{1\rho}$'s were measured between 313 and 243 K on six membrane samples with and without amantadine. The activation energy $E_a$, correlation time prefactor $\tau_0$, and correlation time $\tau$ were extracted by least-square linear fits of the $\ln\left(T_{1\rho}^{-1}\right)$ to 1,000/*T* curves on the high temperature side using (8–9). For the apo VAIL sample, artificially high $T_{1\rho}$ values were observed at 313 K, thus the apo and amantadine-bound VAIL-M2TMP data analysis did not include the 313 K data.

C–H dipolar order parameters were measured at 313 K under 7,000 Hz MAS using a dipolar-doubled DIPSHIFT experiment (Hong et al. 1997) where $^1H$ homonuclear decoupling was achieved by the frequency-switched Lee-Goldburg sequence (Bielecki et al. 1990). The dipolar-doubled sequence suppresses the apparent $T_2$ relaxation by making the total homonuclear decoupling time constant at one rotor period. The $t_1$ evolution time was controlled by the position of a $^{13}C$ $\pi$ pulse in the rotor period.

## Theory

The membrane protein rotational diffusion of interest generally occurs on the microsecond time scale based on the 2D Brownian diffusion theory (Saffman and Delbruck 1975). Motions on this time scale can be probed by $^1H$-decoupled *S*-spin spin–spin relaxation times ($T_2$) and rotating-frame spin-lattice relaxation times ($T_{1\rho}$). The $T_2$ relaxation times of an *S* spin dipolar coupled to an *I* spin under conditions of random isotropic motion and *I* spin rf decoupling depends on the spectral density at the decoupling field strength (Rothwell and Waugh 1981), which is typically 50–100 kHz. However, measurement of $^{13}C$ $T_2$ by the Hahn-echo experiment in uniformly $^{13}C$-labeled residues in proteins has the shortcoming that $^{13}C$–$^{13}C$ scalar

coupling contributes to the time-dependent intensity decay, unless a selective $^{13}C$ $\pi$ pulse is applied to remove the scalar interaction. Given the small chemical shift dispersion among the aliphatic carbons in proteins, very soft $\pi$ pulses, which necessitate multiple experiments with shifted $^{13}C$ offsets, would be required to obtain homonuclear and heteronuclear decoupled $^{13}C$ $T_2$'s of all sites. A simpler alternative, then, for probing microsecond time scale motion is to measure the $T_{1\rho}$, since it is primarily sensitive to spectral densities at the frequency of the spin-lock field (Schaefer et al. 1977), which is also 50–100 kHz.

To obtain site-specific relaxation times, we measure the $^1H$ $T_{1\rho}$ through the directly bonded $^{13}C$ sites by transferring the $^1H$ magnetization to $^{13}C$, and by using spin-diffusion-free Lee-Goldburg spin lock instead of transverse spin lock (van Rossum et al. 2000). The effective spin lock field is thus tilted at the magic angle, $\cos^{-1}(1/\sqrt{3})$, from the static magnetic field. The $^1H$ magnetization, prepared along the direction of the spin-lock field (Fig. 1), can only undergo spin-lattice relaxation in the rotating frame.

The $^1H$ $T_{1\rho}$ relaxation in $^{13}C$-labeled molecules is driven by fluctuating $^1H$–$^1H$ and $^1H$–$^{13}C$ dipolar couplings due to random molecular motions. The orientation-dependent relaxation rate depends on spectral densities, $J(\omega)$, at the spin lock field $\omega_e$, $2\omega_e$, Larmor frequencies $\omega_H$, $\omega_C$, and the sum and difference of $\omega_H$ and $\omega_C$ (Huster et al. 2001; Mehring 1983). Since the Larmor frequencies are three to four orders of magnitude larger than $\omega_e$ ($\omega_H = 2\pi \times 600$ MHz, $\omega_C = 2\pi \times 150$ MHz, and $\omega_e = 2\pi \times 61.2$ kHz in our experiments), for motions in the tens to hundreds of kilohertz regime, one can safely ignore the spectral density terms at the Larmor frequencies. Taking into account MAS at a frequency $\omega_R$, the powder averaged $T_{1\rho}$ for the rotating-frame relevant part is (Fares et al. 2005):

$$\left\langle T_{1\rho}^{-1} \right\rangle = \Delta M_2(S, \delta_{CH}, \delta_{HH}, \beta) \cdot [J(2\omega_e + 2\omega_R) + J(2\omega_e - 2\omega_R) + J(2\omega_e + \omega_R) + J(2\omega_e - \omega_R)] \quad (1)$$

Here $\Delta M_2$ is the product of the dynamic portion of the dipolar second moment and orientational terms that transform spin interaction tensors from their molecule-fixed principal axis frames to the rotor frame (Fares et al. 2005). The dynamic portion of the dipolar second moment is approximately $(1 - S^2)$ times the rigid-limit dipolar second moment, where the order parameter $S$ represents the orientation-invariant part of the interaction. In solid-state NMR, the order parameter can be independently measured by various dipolar chemical-shift correlation experiments (Hong et al. 2002; Huster et al. 2001; Schmidt-Rohr et al. 1992). The dependence of $\Delta M_2$ on the C–H ($\delta_{CH}$) and H–H ($\delta_{HH}$) dipolar couplings in (1) reflects the fact that the $^{13}C$-detected $^1H$ $T_{1\rho}$ relaxation is driven by C–H and H–H dipolar couplings. $\beta$ is the angle between $B_0$ and the spin-lock field and is $\cos^{-1}(1/\sqrt{3})$ in our experiments.

For motions with a single correlation time $\tau$, the spectral density is given by (Lipari and Szabo 1982):

$$J(\omega_i) = \frac{\tau}{1 + \omega_i^2 \tau^2}, \quad (2)$$

Explicitly writing the spectral density terms in (1), we obtain

$$\left\langle T_{1\rho}^{-1} \right\rangle = \Delta M_2(S, \delta_{CH}, \delta_{HH}, \beta) \times \left[ \frac{\tau}{1 + (2\omega_e + 2\omega_R)^2 \tau^2} + \frac{\tau}{1 + (2\omega_e - 2\omega_R)^2 \tau^2} + \frac{\tau}{1 + (2\omega_e + \omega_R)^2 \tau^2} + \frac{\tau}{1 + (2\omega_e - \omega_R)^2 \tau^2} \right] \quad (3)$$

The dependence of $T_{1\rho}$ on correlation time $\tau$ can be considered in three regimes. In the long correlation time or strong collision limit where $2\omega_e\tau \gg 1$, Eq. 3 is approximated as:

$$\left\langle T_{1\rho}^{-1} \right\rangle = \Delta M_2(S, \delta_{CH}, \delta_{HH}, \beta) \times \left[ \frac{1}{(2\omega_e + 2\omega_R)^2} + \frac{1}{(2\omega_e - 2\omega_R)^2} \cdot + \frac{1}{(2\omega_e + \omega_R)^2} + \frac{1}{(2\omega_e - \omega_R)^2} \right] \cdot \frac{1}{\tau}, \quad 2\omega_e\tau \gg 1, \quad (4)$$

In the short correlation time or weak collision regime, (3) is simplified to:

$$\left\langle T_{1\rho}^{-1} \right\rangle = 4\Delta M_2(S, \delta_{CH}, \delta_{HH}, \beta) \cdot \tau, \quad 2\omega_e\tau \ll 1 \quad (5)$$

In the intermediate motional regime where $2\omega_e\tau = 1$, for $\omega_e \gg \omega_R$, the relaxation rate is the fastest, corresponding to a $T_{1\rho}$ minimum:

$$\left\langle T_{1\rho}^{-1} \right\rangle = 2\Delta M_2(S, \delta_{CH}, \delta_{HH}, \beta) \cdot \tau, \quad 2\omega_e\tau = 1 \quad (6)$$

For an activated motional process, the correlation time is given by the Arrhenius law:

$$\tau = \tau_0 \, e^{E_a/RT}, \quad (7)$$

where $E_a$ is the activation energy and $\tau_0$ is the prefactor describing the attempt rate of motion. The larger the attempt rate, the smaller the $\tau_0$, and the shorter the correlation time $\tau$. Substituting $\tau$ into (5), we find that $E_a$ can be extracted from a plot of $\ln\left(T_{1\rho}^{-1}\right)$ versus 1,000/$T$ in the short $\tau$ limit:

$$\ln\left\langle T_{1\rho}^{-1}\right\rangle = \ln(4\Delta M_2\tau_0) + \frac{E_a}{1000\,R}\cdot\frac{1000}{T}, \quad 2\omega_e\tau \ll 1 \tag{8}$$

Equation 8 indicates that the natural logarithm of relaxation rates is linear with 1,000/$T$ with a slope of $E_a$/1,000 $R$ in the short correlation time regime. Moreover, the pre-exponential factor $\tau_0$ can be extracted from the intercept of the linear fit. For this purpose, we use the second moment expression from Mehring (1983), which takes into account both C–H and H–H dipolar relaxation as well as the LG spin lock factor (Huster et al. 2001):

$$4\Delta M_2\tau_0 = (1-S^2)\left(\frac{3}{10}\delta_{\mathrm{HH}}^2 + \frac{1}{15}\delta_{\mathrm{CH}}^2\right)\tau_0, \quad 2\omega_e\tau \ll 1 \tag{9}$$

The motional correlation time is fully determined once the activation energy $E_a$ and the pre-exponential factor $\tau_0$ are obtained from the slope and the intercept, respectively.

In principle, an alternative method to determine the pre-exponential factor $\tau_0$ is to exploit the $T_{1\rho}$ minimum temperature, where $2\omega_e\tau = 1$. However, as we show below, the $T_{1\rho}$ minima observed for membrane-bound M2TMP result from the lipid phase transition, and are thus not the true minima of a single motional process. On the other hand, the lipid-induced $T_{1\rho}$ minima should not affect the high-temperature slopes or intercepts, thus the activation energy $E_a$ and $\tau_0$ can still be extracted reliably from these features.

The $T_{1\rho}$ in the long correlation time limit can in principle also be used to extract $E_a$ and $\tau$. Equations 4 and 5 indicate that the slope of the $\ln\left(T_{1\rho}^{-1}\right)$ plot with 1/$T$ on the low temperature side has the same magnitude but the opposite sign from that of the high temperature side. But this scenario is true only if a single motional process with the same $E_a$ persists throughout the temperature range. Thus, the lipid phase transition makes this assumption invalid. Since our purpose is to understand the physiological temperature dynamics of M2TMP, below we will analyze only the high temperature regime of the $T_{1\rho}$ data to extract M2TMP motional parameters.

## Results

Site-specific $^1$H $T_{1\rho}$ relaxation times were measured on six membrane samples with three sets of labeled residues (LAGI, VAIL, and VSL) without and with amantadine. The eleven labeled residues are distributed from position 26 to 38 in the transmembrane domain, with I32 and H37 being the only residues not measured in this range.

Figure 2 shows representative $^{13}$C spectra of LAGI-M2TMP in the apo- and amantadine-bound states at 313, 273 and 243 K. At 313 K, the amantadine-bound peptide has narrower linewidths than the apo peptide, whereas at 243 K the peptide signals of the two samples have similar intensities and linewidths, indicating immobilization of both states of the peptide. At 273 K, both the apo and bound peptide spectra exhibit significant exchange broadening with very low $^{13}$C intensities. This broadening coincides with the gel to liquid-crystalline phase transition temperature (271 K) of the DLPC membrane, indicating that the M2TMP motion responsible for the exchange broadening is intimately associated with the phase property of the lipid bilayer. The VAIL and VSL spectra exhibit similar temperature dependences and are given in the Supporting Information (Figs. S1, S2). The fact that the amantadine-bound samples show narrower and higher backbone Cα signals than the apo samples at high temperature (Cady and Hong 2008) indicates dynamic differences induced by amantadine, the nature of which are analyzed below.

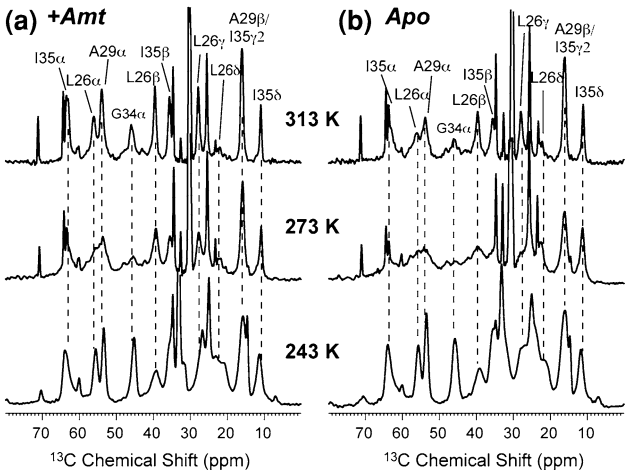


**Fig. 2** 1D $^{13}$C CP-MAS spectra of LAGI M2TMP in DLPC bilayers at 313, 273, and 243 K. **a** With amantadine, **b** without amantadine

$^1$H $T_{1\rho}$ were measured at six to seven temperatures between 313 and 243 K. Figure 3 displays representative $T_{1\rho}$ decay curves at 313, 273, and 243 K as a function of spin-lock time. The decay curves are well fit by single exponential functions, where the decay constants correspond to $T_{1\rho}$. At 313 K, the $T_{1\rho}$ decays are slower for the amantadine-bound peptide than for the apo peptide for all residues, indicating the bound peptide has longer $T_{1\rho}$'s. At 273 K, the $^1$H $T_{1\rho}$'s are significantly shorter than the high-temperature values for both the apo and bound peptides, and the bound peptide has marginally longer $T_{1\rho}$'s than the apo peptide. At 243 K, the $T_{1\rho}$ values increase significantly over the high temperature values, and there is no longer a consistent difference between the apo and bound peptide. Supporting information Tables S1–S3 lists all $T_{1\rho}$ values

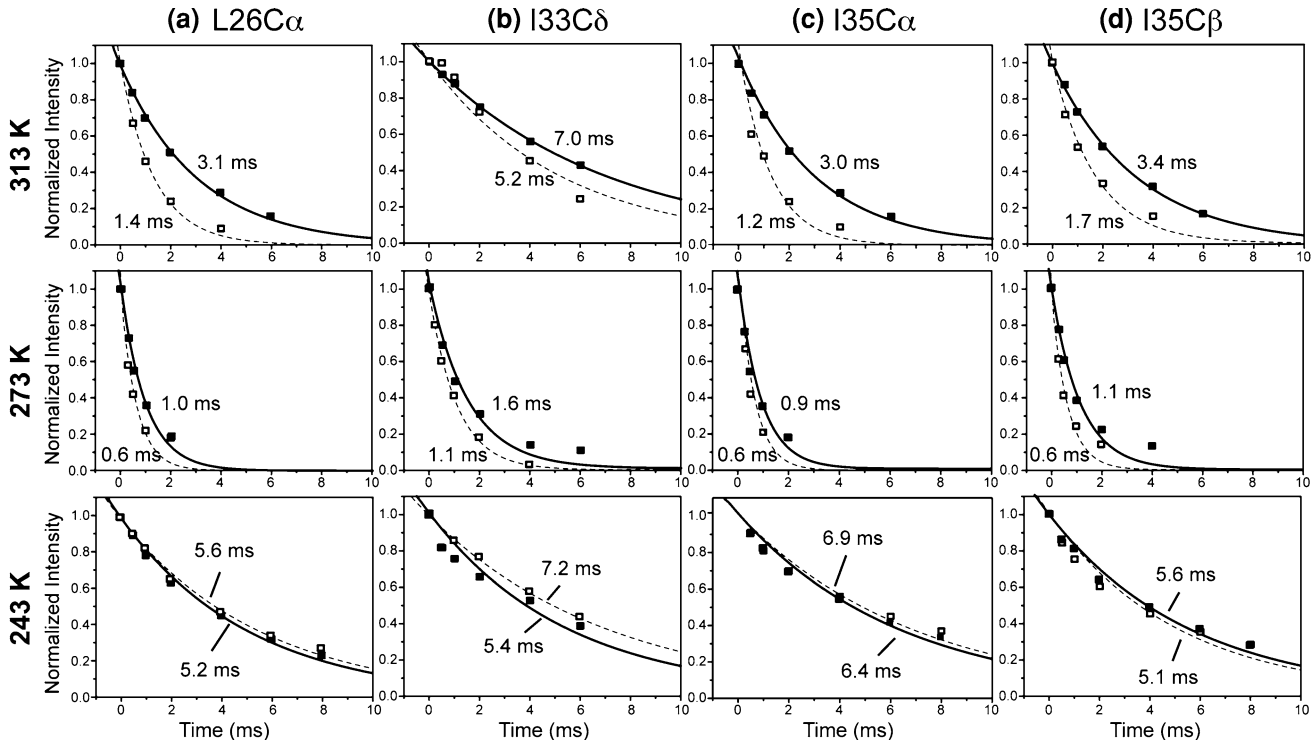


**Fig. 3** Representative $^{1}$H $T_{1\rho}$ relaxation decays of M2TMP in DLPC bilayers at 313, 273, and 243 K. **a** L26 Cα, **b** I33 Cδ, **c** I35 Cα, and **d** I35 Cβ. The apo data are shown as *open squares* and fit by *dashed lines*. The amantadine-bound data are shown as *filled squares* and fit by *solid lines*. The decay constants are indicated for all sites

for backbone Hα, sidechain Hβ, and sidechain methyl protons in the apo and bound M2TMP at all temperatures.

Figure 4 shows the $^{1}$H $T_{1\rho}$'s as a function of 1,000/$T$ ($K^{-1}$) for representative backbone and sidechain sites. All curves have a "V" shape, indicative of passage through the fastest relaxing intermediate motional regime. Between the apo and bound peptides, the minimum $T_{1\rho}$ positions match well, with relatively similar $T_{1\rho}$ values as well as the transition temperature $T_c$. On the high temperature side of the minimum, the bound peptide has progressively longer $T_{1\rho}$'s than the apo peptide with increasing temperature, indicating that M2TMP has shorter correlation times in the presence of amantadine (5). On the low temperature side, the apo and bound peptides have smaller $T_{1\rho}$ differences for the small number of temperatures measured.

To quantify the amantadine-induced dynamic differences of M2TMP, we convert the $T_{1\rho}$ plots to $\ln\left(T_{1\rho}^{-1}\right)$ and extract the activation energy and correlation time prefactor $\tau_0$ using (8–9). Figure 5 shows $\ln\left(T_{1\rho}^{-1}\right)$ as a function of 1,000/$T$ for a number of Hα sites. As expected, the shapes of the plots are roughly inverted from those of Fig. 4, with the amantadine-bound peptide showing smaller relaxation rates than the apo peptide at physiological temperature. On the high temperature side of the $T_{1\rho}$ minimum, $\ln\left(T_{1\rho}^{-1}\right)$ is roughly linear with inverse temperature for most sites, thus

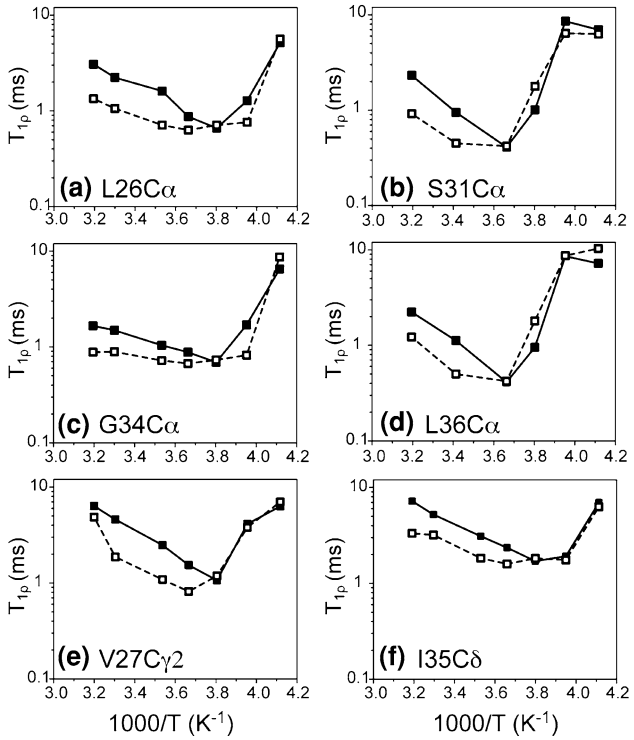


**Fig. 4** $^{1}$H $T_{1\rho}$ versus 1,000/$T$ for representative M2TMP Cα sites in the apo (*open squares* and *dashed line*) and amantadine-bound (*closed squares* and *solid line*) states in DLPC bilayers. **a** L26 Cα, **b** S31 Cα, **c** G34 Cα, **d** L36, **e** V27 Cγ2, **f** I35 Cδ

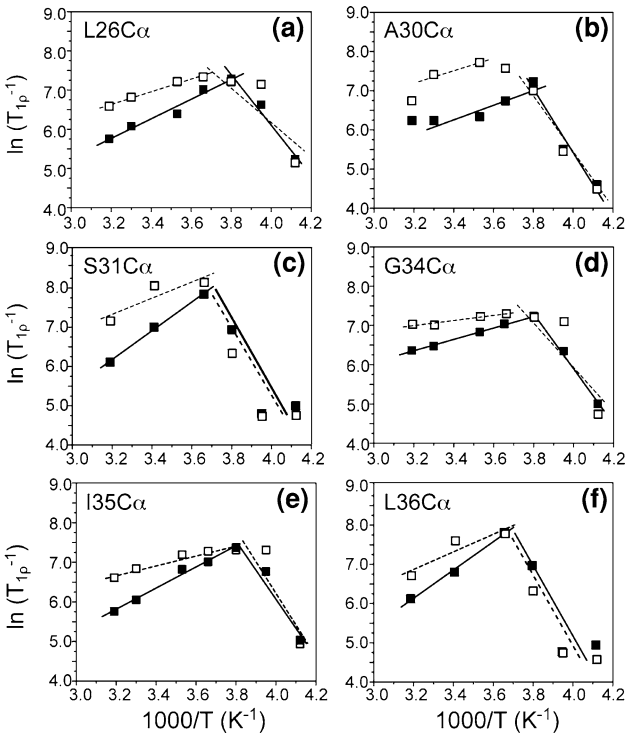


**Fig. 5** $\ln\left(T_{1\rho}^{-1}\right)$ versus 1,000/$T$ curves for representative Cα sites of M2TMP. **a** L26, **b** A30, **c** S31, **d** G34, **e** I35, **f** L36. The apo data are shown as *open squares* and fit by *dashed lines*, and the amantadine-bound data are shown as *filled squares* and fit by *solid lines*

supporting the assumption that the rotational diffusion can be regarded as an activated process (vide infra). Moreover, the amantadine-bound peptide has more positive slopes than the apo peptide, indicating larger $E_a$. Least-square linear fits of the high-temperature side of the $\ln\left(T_{1\rho}^{-1}\right)$ curves yielded the activation energies, listed in Table 1. The amantadine-bound peptide has an average $E_a$ of 23.3 kJ/mol, which is 66% larger than the average $E_a$ of 14.0 kJ/mol for the apo peptide. The average experimental uncertainty of the $E_a$ is 17%. The standard deviation of the $E_a$ distributions is 6.2 kJ/mol for the bound peptide and 4.2 kJ/mol for the apo peptide. Figure 6 compares the $E_a$ values of the apo and bound peptides for each Hα site. With the exception of G34, the $E_a$'s are relatively uniform across all residues, given the experimental uncertainty. The small $E_a$ distribution is consistent with the approximation that the main motional process driving $T_{1\rho}$ relaxation is whole-body uniaxial diffusion rather than segmental motion. In addition, the $E_a$ ratio between the bound and apo peptides for each site is relatively uniform, with an average ratio of 1.73 and a standard deviation of 0.35.

To obtain the motional correlation times, we need the C–H order parameters and $E_a$ (7, 9). The Cα–Hα order parameters (Table 1) are found to be similar between the apo and bound peptides, indicating that the amantadine-induced spectral line narrowing is not due to amplitude changes but due to rate changes. Using the high-temperature intercepts and $S_{CH}$, we calculated $\tau_0$ and $\tau_{313\ K}$ for the apo and amantadine-bound M2TMP (Table 1). The bound peptide exhibits smaller $\tau_0$ values, indicating higher attempt rates. As a result, the average $\tau_{313\ K}$ is shorter for the bound peptide (0.89 ± 0.41 μs) than the apo peptide (2.8 ± 0.9 μs). The threefold reduction of $\tau_{313\ K}$ in the presence of amantadine is qualitatively consistent with the twofold longer $T_{1\rho}$, since $T_{1\rho}^{-1}$ is linear with $\tau$ in the short $\tau$ regime (5). The magnitude of $\tau_{313\ K}$ is also reasonable, as it is similar to or shorter than the inverse of the spin lock field of 2.7 μs. In other words, the amantadine-bound M2TMP

**Table 1** $E_a$, $\tau_0$, and $\tau_{313\ K}$ of M2TMP in DLPC bilayers in the absence and presence of amantadine extracted from Hα $T_{1\rho}$'s

| Residue | Amantadine-bound peptide | | | | | Apo peptide | | | | |
|---|---|---|---|---|---|---|---|---|---|---|
| | $E_a$ (kJ/mol) | $\tau_0$ (ns) | $\tau_{313\ K}$ (μs) | $T_{1\rho}^{313\ K}$ (ms) | $S_{CH}$ | $E_a$ (kJ/mol) | $\tau_0$ (ns) | $\tau_{313\ K}$ (μs) | $T_{1\rho}^{313\ K}$ (ms) | $S_{CH}$ |
| L26 | $20.9^{1.3}$ | 0.25 | 0.76 | $3.1^{0.1}$ | $0.42^{0.02}$ | $13.5^{1.3}$ | 10.3 | 1.9 | $1.3^{0.1}$ | $0.44^{0.02}$ |
| V27 | $25.1^{7.8}$ | 0.03 | 0.40 | $4.0^{0.3}$ | $0.33^{0.04}$ | $17.1^{-}$ | 3.8 | 2.8 | $1.4^{0.1}$ | $0.31^{0.02}$ |
| V28 | $32.4^{5.4}$ | 0.004 | 1.07 | $2.6^{0.3}$ | $0.46^{0.04}$ | $18.3^{6.2}$ | 2.1 | 2.4 | $1.2^{0.1}$ | $0.46^{0.04}$ |
| A29 | $21.7^{1.3}$ | 0.18 | 0.76 | $3.5^{0.1}$ | $0.44^{0.02}$ | $17.5^{1.3}$ | 1.7 | 1.4 | $1.7^{0.1}$ | $0.46^{0.02}$ |
| A30 | $15.9^{4.7}$ | 2.32 | 4.3 | $1.9^{0.2}$ | $0.60^{0.02}$ | $11.0^{-}$ | 62.9 | 1.1 | $1.2^{0.1}$ | $0.60^{0.07}$ |
| S31 | $30.7^{7.8}$ | 0.0086 | 1.1 | $2.3^{0.3}$ | $0.50^{0.02}$ | $13.6^{7.2}$ | 15.0 | 2.8 | $0.9^{0.1}$ | $0.40^{0.02}$ |
| I33 | $25.1^{1.8}$ | 0.027 | 0.40 | $4.0^{0.3}$ | $0.46^{0.02}$ | $17.1^{-}$ | 4.4 | 3.2 | $1.4^{0.1}$ | $0.31^{0.02}$ |
| G34 | $12.1^{0.4}$ | 17.5 | 1.8 | $1.7^{0.1}$ | $0.60^{0.02}$ | $5.4^{0.9}$ | 514 | 4.1 | $0.9^{0.1}$ | $0.69^{0.09}$ |
| I35 | $22.2^{1.3}$ | 0.16 | 0.79 | $3.1^{0.1}$ | $0.42^{0.02}$ | $12.0^{1.3}$ | 18.0 | 1.9 | $1.3^{0.1}$ | $0.42^{0.02}$ |
| L36 | $30.2^{2.1}$ | 0.010 | 1.1 | $2.2^{0.2}$ | $0.48^{0.04}$ | $18.6^{8.1}$ | 1.8 | 2.3 | $1.2^{0.1}$ | $0.44^{0.02}$ |
| L38 | $20.6^{9.9}$ | 0.18 | 0.48 | $2.9^{0.2}$ | $0.35^{0.02}$ | $9.6^{-}$ | 96.6 | 3.8 | $1.3^{0.1}$ | $0.33^{0.07}$ |
| Mean | 23.3 ± 6.2 | | 0.89 ± 0.41 | 2.8 ± 0.8 | | 14.0 ± 4.2 | | 2.8 ± 0.9 | 1.3 ± 0.2 | |

The 313 K $T_{1\rho}$ and $S_{CH}$ are also listed along with their uncertainties (superscript)

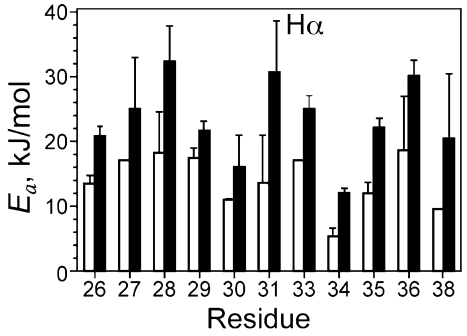


**Fig. 6** Activation energy $E_a$ (kJ/mol) extracted from the high-temperature slopes of the Hα $\ln\left(T_{1\rho}^{-1}\right)$ versus 1,000/$T$ curves. The amantadine-bound M2TMP (*filled bars*) has larger activation energies than the apo peptide (*open bars*)

has a shorter correlation time than the characteristic time scale of the spin-lock field, thus alleviating exchange broadening, while the apo peptide correlation time is closer to the NMR time scale, thus giving rise to broader lines. Decreasing the temperature to 273 K increased the $\tau$ to 6.0 μs and 3.4 μs for the apo and bound peptides, respectively.

It is also interesting to examine the sidechain $^1$H $T_{1\rho}$ trends. Table S3 shows that the methyl proton $T_{1\rho}$'s are much longer than the backbone Hα $T_{1\rho}$'s and are relatively similar between the apo and bound peptides at high temperatures. Figure 7 shows representative $\ln\left(T_{1\rho}^{-1}\right)$ plots of two methyl groups and one methine Cβ site. The methyl protons have more similar high-temperature slopes between the apo and bound peptides, with an apparent activation energy difference of only 20% between the two states. The similarities can be attributed to three-site jumps of the methyl groups that are additional to the uniaxial diffusion, which reduce the dynamic difference between the apo and bound peptide. In comparison, the Cβ sites show more distinct activation energies between the apo and bound states, consistent with the Hα $T_{1\rho}$ behavior.

## Discussion

### M2TMP uniaxial diffusion is the main motion driving $T_{1\rho}$ relaxation

The motivation for this work is to quantify the motion of M2TMP that is responsible for exchange broadening of its NMR spectra in phosphocholine bilayers at physiological temperatures, and to understand the origin of amantadine-induced line narrowing.

The exchange broadening is due to microsecond motion of the peptide that interferes with $^{13}$C–$^1$H and $^{15}$N–$^1$H dipolar decoupling and cross polarization. We assign the motion to whole-body uniaxial rotational diffusion of the M2 helical bundle. The presence of this uniaxial diffusion has been previously shown based on the lineshapes of $^2$H quadrupolar spectra, $^{15}$N static powder spectra, and $^{15}$N–$^1$H and $^{13}$C–$^1$H dipolar couplings (Cady et al. 2007). Two lines of evidence support the assignment of the $T_{1\rho}$ relaxation mechanism to this uniaxial diffusion. First, all eleven measured residues exhibit rapid $T_{1\rho}$ relaxation at high temperatures, and all $T_{1\rho}$ values are increased by amantadine. Such across-the-board effects can only result from a whole-body motion. Second, the two-dimensional Brownian diffusion theory of Saffman and Delbrück predicts a rate of $10^5$/s for the uniaxial diffusion of the M2 helical bundle, which agrees well with the time scale probed by the $T_{1\rho}$ experiments.

The presence of whole-body motion does not exclude additional internal motions. Sidechain motions are certainly present, although they do not interfere with the extraction of the rates and activation energy of uniaxial diffusion from the backbone Hα $T_{1\rho}$ data. The clearest manifestation of sidechain motions is the fact that the methyl protons have longer $T_{1\rho}$'s than the backbone protons, and the methyl $^1$H $T_{1\rho}$'s are similar between the apo and bound peptides at high temperatures (Table S3). These observations are not surprising, since the fast methyl

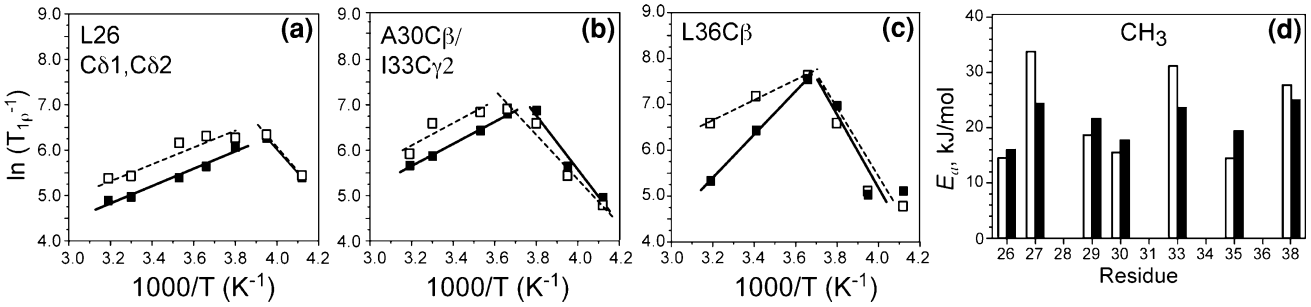


**Fig. 7** **a–c** $\ln\left(T_{1\rho}^{-1}\right)$ versus 1,000/$T$ curves for several M2TMP sidechains. **a** L26 methyl Cδ1/ Cδ2, **b** A30 Cβ and I33 Cγ2 methyl groups. **c** L36 Cβ. Apo data: *open squares* and *dashed lines*. Amantadine-bound data: *filled squares* and *solid lines*. **d** Activation energy (kJ/mol) of the methyl protons. The average $E_a$ difference between the apo and bound peptides is ~20%

rotation on the nanosecond time scale pre-averages the dipolar second moment, and thus reduce the relaxation rates (1). The local nature of the methyl rotation also makes the motion less sensitive to amantadine binding. The full $T_{1\rho}$ dependence includes spectral densities at the $^{1}$H and $^{13}$C Larmor frequencies, which are more relevant time scales for the methyl rotation. Thus, (1) does not apply fully to methyl groups. Since the main purpose of this study is to understand the motion that causes exchange broadening of the NMR spectra, but sidechain methyl $^{13}$C signals do not suffer from exchange broadening, we do not consider the combined motion of three-site jumps and uniaxial diffusion experienced by the methyl groups further. Another manifestation of possible segmental motions is the distribution of $E_a$. Specifically, the G34 $E_a$ is two standard deviations lower than the average, suggesting the local motion at this residue (vide infra).

## Correlation time of M2TMP diffusion and origin of spectral line narrowing by amantadine

The threefold shorter correlation time of the amantadine-bound M2TMP (Table 1) explains the amantadine-induced line narrowing of the peptide spectra. The faster motional rates better avoid the intermediate time scale condition, thus alleviating line broadening. The faster diffusion rates result from the one to two orders of magnitude reduction of the prefactor $\tau_0$, as obtained from the high-temperature intercepts of the $\ln\left(T_{1\rho}^{-1}\right)$ curves. The intercept depends both on $\tau_0$ and the dipolar second moment (9), whose exact magnitude differs somewhat between different theories, depending on how many spin interactions are included and whether the MAS or the static condition is operative (Fares et al. 2005; Huster et al. 2001; Mehring 1983). However, the ratio of the intercepts between the apo and bound peptide depends only on $\tau_0$. Thus, the relative size of $\tau_0$ between the apo peptide (long $\tau_0$) and the bound peptide (short $\tau_0$) is unambiguous.

The shorter $\tau_0$ of the amantadine-bound M2TMP indicates higher attempt rates of motion, which suggest that the M2 helices form better-packed tetramers in the presence of amantadine. Amantadine may interact with all four helices of the tetramer, thus serving as a non-covalent linker that brings the four helices together to form a more cohesive tetrameric bundle. A more cohesive helical bundle can diffuse faster, and would also have structurally and dynamically more homogeneous individual helices. This interpretation is consistent with the relative lack of correlation time distribution for the bound peptide (vide infra), as manifested by the sharpness of the $T_{1\rho}$ minima, and is also consistent with disulfide cross linking data that indicate increased tetramer association in the presence of amantadine (Cristian et al. 2003). Thus, the reduced $\tau_0$ of the bound M2TMP suggests that amantadine is centrally located in the pore of the channel, shared by all four helices, consistent with the binding site seen in a recent crystal structure (Stouffer et al. 2008). In comparison, a solution NMR study (Schnell and Chou 2008) found four rimantadine molecules at the lipid-facing surface of each channel. It is difficult to imagine how this surface binding motif would homogenize the peptide conformation and speed up its motion.

A question that is beyond the scope of the current study is the correlation time distribution of apo M2TMP, which is manifested by the broad $T_{1\rho}$ minima of the apo peptide. The $\tau$ distribution suggests that without amantadine, the M2 helical bundles are floppier, with more internal degrees of freedom, and may exhibit dynamic heterogeneities between different tetramers. Such dynamic heterogeneity may be functionally relevant, as it may allow the apo peptide to adopt appropriate conformations to achieve its many functions, including channel activation, gating, and inhibition.

## The activation energy of M2TMP uniaxial diffusion is related to membrane viscosity

A basic assumption in our dynamic analysis is that the rotational diffusion of a membrane protein in lipid bilayers can be considered an activated process that follows an Arrhenius law (7). The linearity of the observed $\ln\left(T_{1\rho}^{-1}\right)$ with respect to 1,000/$T$ at high temperatures (Fig. 5) validates this assumption, but it is of interest to consider the physical basis for the activated diffusion. Membrane protein diffusion in lipid bilayers requires the availability of free volume in the vicinity of the protein, which is achieved by discrete hopping of the lipid molecules. Thus, activated lateral and rotational diffusion of membrane proteins has its molecular origin in the free volume theory of liquids (Cohen and Turbill 1959; Galla et al. 1979). Considered in this light, the activation energy essentially reflects the macroscopic viscosity of the membrane. Higher activation

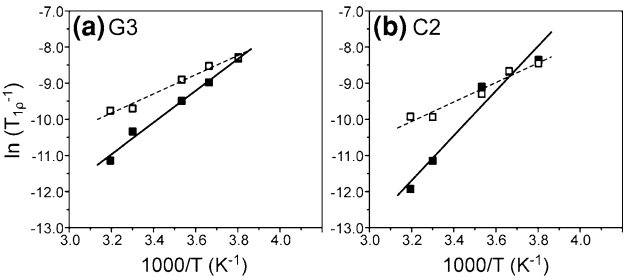


**Fig. 8** $ln\left(T_{1\rho}^{-1}\right)$ versus 1,000/$T$ curves for several lipid $^{13}$C signals in M2TMP-containing DLPC bilayers. **a** Glycerol backbone G3. **b** Acyl chain C2. Apo data: *open squares* and *dashed lines*; Amantadine-bound data: *filled squares* and *solid lines*

energies indicate higher viscosities. Thus, the higher $E_a$ of the amantadine-bound peptide indicates that excess amantadine increases the membrane viscosity. If this is true, then the lipid $^1$H $T_{1\rho}$ values should be affected by the excess amantadine outside the channel in the bilayer, in the same manner as the protein.

Examination of several resolved lipid $^{13}$C signals confirms that there is indeed an amantadine-induced increase of the lipid $E_a$. Figure 8 shows the $\ln\left(T_{1\rho}^{-1}\right)$ curves of the lipid glycerol G3 and the acyl chain C2 signals. The excess-amantadine-containing membrane clearly has larger slopes than the amantadine-free membrane, similar to the peptide $T_{1\rho}$ behavior. The amantadine-bound samples in our experiments contain eightfold molar excess of amantadine to the peptide, or 32-fold excess amantadine to the channel. The excess amantadine partitions into the bilayer (Subczynski et al. 1998; Wang et al. 2004). Paramagnetic relaxation enhancement NMR data indicate that amantadine is located at the interfacial region of the DMPC bilayer with the amine group pointing to the surface (Li et al. 2008). This depth and orientation are consistent with the amphipathic nature of amantadine, with its hydrophobic adamantane cage close the hydrocarbon core and its polar ammonium moiety pointing to the polar region of the bilayer.

Our recently measured lipid $^{13}$C $T_2$ relaxation times at 313 K in peptide-free DLPC bilayers showed no discernible difference between amantadine-containing and amantadine-free bilayers (Cady et al. 2009), in contrast to the current lipid $^1$H $T_{1\rho}$ data. This discrepancy is likely due to the presence of the peptide in the current measurements but the lack of the peptide in the previous $T_2$ experiments. Membrane viscosity is a function of molecular crowding: peptide-containing bilayers have much smaller free volumes for amantadine than pure lipid bilayers, thus amantadine may cause detectable fluidity changes only in M2-containing bilayers.

The viscosity origin of the activation energy of M2TMP diffusion also explains the asymmetric slope of the $\ln\left(T_{1\rho}^{-1}\right)$ curves on the two sides of the $T_{1\rho}$ minimum. Both the apo and bound peptides have steeper slopes or larger apparent activation energies on the low temperature side. Since this $T_{1\rho}$ minimum is associated with phase transition of the DLPC bilayer, the slope increase at low temperature is caused by the significant viscosity increase of the gel-phase membrane compared to the liquid-crystalline phase. Thus, the M2TMP rotational diffusion is not a single motional process above and below the lipid phase transition temperature, in contrast to most other motions that have been characterized by NMR (Douglass and Jones 1966; Rothwell and Waugh 1981).

The viscosity origin of the activation energy may also partly explain the $E_a$ distribution among the residues. Since a perfectly rigid-body motion should have a single $E_a$, the observed $E_a$ distribution beyond the experimental uncertainty must reflect additional motions, which may result from varying membrane viscosity across the bilayer thickness. The abnormally low $E_a$ of G34 may then be partly due to the location of G34 at the center of the TM helix and thus at the center of the bilayer, which has the lowest viscosity due to large-amplitude motions of the lipid chain ends. While the exact nature of the local G34 motion is unknown, the conclusion of increased conformational flexibility is consistent with a large number of NMR parameters for this site: its $^{15}$N anisotropic chemical shifts, N–H dipolar coupling (Hu et al. 2007), and $^{15}$N isotropic chemical shifts were all found to change with drug binding (Cady et al. 2009; Wang et al. 2009) and membrane composition (Luo et al. 2009).

The lipid-mediated influences of excess amantadine on the diffusion dynamics of M2TMP do not change the previous conclusion that the protein-bound amantadine causes site-specific conformational changes through direct amantadine-protein interactions. The structural changes are manifested as chemical shift perturbations that are highly site specific, with residues S31, G34, and V28 exhibiting large chemical shift perturbations while other residues showing little changes (Cady and Hong 2008; Cady et al. 2009).

## Conclusion

The temperature-dependent $^1$H $T_{1\rho}$ relaxation times shown here indicate that the uniaxial diffusion of the M2TMP in liquid-crystalline DLPC bilayers causes efficient $^1$H $T_{1\rho}$ relaxation, and the diffusion rates are increased by amantadine through an increase in the attempt frequencies. The average motional correlation time at 313 K is 0.89 μs for the bound peptide and 2.8 μs for the apo peptide. The faster diffusion of the bound peptide suggests that amantadine induces more homogeneous and better-packed M2TMP tetramers by coordinating with all four helices. Thus, the well documented amantadine-induced NMR line narrowing is due to suppression of the intermediate time scale broadening.

From the linear relation of $\ln\left(T_{1\rho}^{-1}\right)$ with $1/T$ at high temperature, we extracted the activation energy of the M2 uniaxial diffusion. The average $E_a$ is 23.3 kJ/mol for the bound peptide and 14.0 kJ/mol for the apo peptide. The higher $E_a$ of the bound peptide is attributed to larger membrane viscosity by excess amantadine, which is confirmed by the lipid $T_{1\rho}$ data.

Similar exchange broadening of the apo protein and line narrowing of the bound protein have also been reported for solution NMR spectra of M2 (18–60) in DHPC micelles

(Schnell and Chou 2008). There, the exchange broadening of the apo protein spectra was alleviated by the addition of 40 mM rimantadine. At 53-fold molar excess to the protein (0.75 mM), the excess rimantadine is expected to significantly increase the viscosity of the micelle interior, which may affect the dynamics of the micelle-bound rimantadine in a way that facilitates the observation of its NOEs with the protein.

The present study illustrates the rich information that can be obtained from temperature-dependent relaxation studies of membrane proteins. Compared to most relaxation NMR studies so far, which were targeted to either small molecules with a single motion (Rothwell and Waugh 1981) or macromolecules with a well-defined local motion (Batchelder et al. 1982), the present study examines the rates and energetics of the global motion of a membrane protein (Reuther et al. 2006). It gives a glimpse into the energetic driving force behind membrane protein uniaxial diffusion, which is not easily obtained by other biophysical techniques (Gennis 1989).

## References


Aisenbrey C, Bechinger B (2004) Investigations of polypeptide rotational diffusion in aligned membranes by 2H and 15N solid-state NMR spectroscopy. J Am Chem Soc 126:16676–16683

Batchelder LS, Sullivan CE, Jelinski LW, Torchia DA (1982) Characterization of leucine side-chain reorientation in collagen-fibrils by solid-state 2H NMR. Proc Natl Acad Sci USA 79:386–389

Bielecki A, Kolbert AC, de Groot HJM, Griffin RG, Levitt MH (1990) Frequency-switched Lee-Goldburg sequences in solids. Adv Magn Reson 14:111–124

Bloom M, Evans E, Mouritsen OG (1991) Physical properties of the fluid lipid-bilayer component of cell membranes: a perspective. Q Rev Biophys 24:293–397

Blume A, Rice DM, Wittebort RJ, Griffin RG (1982) Molecular dynamics and conformation in the gel and liquid-crystalline phases of phosphatidylethanolamine bilayers. Biochemistry 21:6220–6230

Cady SD, Hong M (2008) Amantadine-induced conformational and dynamical changes of the influenza M2 transmembrane proton channel. Proc Natl Acad Sci USA 105:1483–1488

Cady SD, Goodman C, Tatko CD, DeGrado WF, Hong M (2007) Determining the orientation of uniaxially rotating membrane proteins using unoriented samples: a 2H, 13C, AND 15N solid-state NMR investigation of the dynamics and orientation of a transmembrane helical bundle. J Am Chem Soc 129:5719–5729

Cady SD, Mishanina TV, Hong M (2009) Structure of amantadine-bound M2 transmembrane peptide of influenza A in lipid bilayers from magic-angle-spinning solid-state NMR: the role of Ser31 in amantadine binding. J Mol Biol 385:1127–1141

Carpino LA, Han GY (1972) The 9-fluorenylmethoxycarbonyl amino-protecting group. J Org Chem 37:3404–3409

Clore GM, Szabo A, Bax A, Kay LE, Driscoll PC, Gronenborn AM (1990) Deviations from the simple 2-parameter model-free approach to the interpretation of N-15 nuclear magnetic relaxation of proteins. J Am Chem Soc 112:4989–4991

Cohen MH, Turbill D (1959) Molecular transport in liquids and glasses. J Chem Phys 31:1164–1169

Cristian L, Lear JD, DeGrado WF (2003) Use of thiol-disulfide equilibria to measure the energetics of assembly of transmembrane helices in phospholipid bilayers. Proc Natl Acad Sci USA 100:14772–14777

deAzevedo ER, Hu WG, Bonagamba TJ, Schmidt-Rohr K (2000) Principles of centerband-only detection of exchange in solid-state nuclear magnetic resonance, and extension to four-time centerband-only detection of exchange. J Chem Phys 112:8988–9001

Douglass DC, Jones GP (1966) Nuclear magnetic relaxation of n-alkanes in rotating frame. J Chem Phys 45:956–963

Fares C, Qian J, Davis JH (2005) Magic angle spinning and static oriented sample NMR studies of the relaxation in the rotating frame of membrane peptides. J Chem Phys 122:194908

Galla HJ, Hartmann W, Theilen U, Sackmann E (1979) On two-dimensional passive random walk in lipid bilayers and fluid pathways in biomembranes. J Membr Biol 48:215–236

Gennis RB (1989) Biomembranes: molecular structure and function. Springer, New York

Glaser RW, Sachse C, Durr UH, Wadhwani P, Ulrich AS (2004) Orientation of the antimicrobial peptide PGLa in lipid membranes determined from 19F-NMR dipolar couplings of 4-CF3-phenylglycine labels. J Magn Reson 168:153–163

Hagemeyer A, Schmidt-Rohr K, Spiess HW (1989) 2D NMR experiments for studying molecular order and dynamics in static and rotating solids. Adv Magn Reson 13:85–130

Hay AJ, Wolstenholme AJ, Skehel JJ, Smith MH (1985) The molecular basis of the specific anti-influenza action of amantadine. EMBO J 4:3021–3024

Hong M (2007) Structure, topology, and dynamics of membrane peptides and proteins from solid-state NMR spectroscopy. J Phys Chem B 111:10340–10351

Hong M, Doherty T (2006) Orientation determination of membrane-disruptive proteins using powder samples and rotational diffusion: a simple solid-state NMR approach. Chem Phys Lett 432:296–300

Hong M, Gross JD, Rienstra CM, Griffin RG, Kumashiro KK, Schmidt-Rohr K (1997) Coupling amplification in 2D MAS NMR and its application to torsion angle determination in peptides. J Magn Reson 129:85–92

Hong M, Yao XL, Jakes K, Huster D (2002) Investigation of molecular motions by Lee-Goldburg cross-polarization NMR spectroscopy. J Phys Chem B 106:7355–7364

Hu J, Asbury T, Achuthan S, Li C, Bertram R, Quine JR, Fu R, Cross TA (2007) Backbone structure of the amantadine-blocked transmembrane domain M2 proton channel from influenza A virus. Biophys J 92:4335–4343

Huster D, Xiao LS, Hong M (2001) Solid-state NMR investigation of the dynamics of the soluble and membrane-bound colicin Ia channel-forming domain. Biochemistry 40:7662–7674

Ishima R, Torchia DA (2000) Protein dynamics from NMR. Nat Struct Biol 7:740–743

Ito T, Gorman OT, Kawaoka Y, Bean WJ, Webster RG (1991) Evolutionary analysis of the influenza A virus M gene with comparison of the M1 and M2 proteins. J Virol 65:5491–5498

Jelinski LW, Sullivan CE, Torchia DA (1980) 2H NMR study of molecular motion in collagen fibrils. Nature 284:531–534

Kay LE (1998) Protein dynamics from NMR. Nat Struct Biol (suppl):513–517

Kinsey RA, Kintanar A, Tsai MD, Smith RL, Janes N, Oldfield E (1981) First observation of amino acid side chain dynamics in membrane proteins using high field deuterium nuclear magnetic resonance spectroscopy. J Biol Chem 256:4146–4149

Kovacs FA, Cross TA (1997) Transmembrane four-helix bundle of influenza A M2 protein channel: structural implications from helix tilt and orientation. Biophys J 73:2511–2517

Lee K-C, Hu W, Cross TA (1993) 2H NMR determination of the global correlation time of the gramicidin channel in a lipid bilayer. Biophys J 65:1162–1167

Lewis BA, Harbison GS, Herzfeld J, Griffin RG (1985) NMR structural analysis of a membrane protein: bacteriorhodopsin peptide backbone orientation and motion. Biochemistry 24: 4671–4679

Li C, Qin H, Gao FP, Cross TA (2007) Solid-state NMR characterization of conformational plasticity within the transmembrane domain of the influenza A M2 proton channel. Biochim Biophys Acta 1768:3162–3170

Li C, Yi M, Hu J, Zhou HX, Cross TA (2008) Solid-state NMR and MD simulations of the antiviral drug amantadine solubilized in DMPC bilayers. Biophys J 94:1295–1302

Lipari G, Szabo A (1982) Model-free approach to the interpretation of nuclear magnetic-resonance relaxation in macromolecules. 1. Theory and range of validity. J Am Chem Soc 104:4546–4559

Luo W, Hong M (2006) Determination of the oligomeric number and intermolecular distances of membrane protein assemblies by anisotropic (1)H-driven spin diffusion NMR spectroscopy. J Am Chem Soc 128:7242–7251

Luo W, Cady SD, Hong M (2009) Immobilization of the influenza A M2 transmembrane peptide in virus-envelope mimetic lipid membranes: a solid-state NMR investigation. Biochemistry 48:6361–6368

Macdonald PM, Seelig J (1988) Dynamic properties of gramicidin A in phospholipid membranes. Biochemistry 27:2357–2364

Mandel AM, Akke M, Palmer AG (1996) Dynamics of ribonuclease H: temperature dependence of motions on multiple time scales. Biochemistry 35:16009–16023

Mehring M (1983) Principles of high resolution NMR in solids. Springer, Berlin

Munowitz M, Aue WP, Griffin RG (1982) Two-dimensional separation of dipolar and scaled isotropic chemical shift interactions in magic angle NMR spectra. J Chem Phys 77:1686–1689

Opella SJ (1986) Protein dynamics by solid state nuclear magnetic resonance. Methods Enzymol 131:327–361

Palmer AG, Williams J, McDermott A (1996) Nuclear magnetic resonance studies of biopolymer dynamics. J Phys Chem 100:13293–13310

Palmer AG, Kroenke CD, Loria JP (2001) Nuclear magnetic resonance methods for quantifying microsecond-to-millisecond motions in biological macromolecules. Methods Enzymol 339:204–238

Park SH, Mrse AA, Nevzorov AA, De Angelis AA, Opella SJ (2006) Rotational diffusion of membrane proteins in aligned phospholipid bilayers by solid-state NMR spectroscopy. J Magn Reson 178:162–165

Pauls KP, MacKay AL, Söderman O, Bloom M, Tanjea AK, Hodges RS (1985) Dynamic properties of the backbone of an integral membrane polypeptide measured by 2H-NMR. Eur Biophys J 12:1–11

Pinto LH, Lamb RA (2007) Controlling influenza virus replication by inhibiting its proton flow. Mol Biosyst 3:18–23

Pinto LH, Holsinger LJ, Lamb RA (1992) Influenza virus M2 protein has ion channel activity. Cell 69:517–528

Prosser RS, Davis JH, Mayer C, Weisz K, Kothe G (1992) Deuterium NMR relaxation studies of peptide-lipid interactions. Biochemistry 31:9355–9363

Reuther G, Tan KT, Vogel A, Nowak C, Arnold K, Kuhlmann J, Waldmann H, Huster D (2006) The lipidated membrane anchor of full length N-Ras protein shows an extensive dynamics as revealed by solid-state NMR spectroscopy. J Am Chem Soc 128:13840–13846

Rothwell WP, Waugh JS (1981) Transverse relaxation of dipolar coupled spin systems under Rf-irradiation—detecting motions in solids. J Chem Phys 74:2721–2732

Saffman PG, Delbruck M (1975) Brownian motion in biological membranes. Proc Natl Acad Sci USA 72:3111–3113

Sakaguchi T, Tu Q, Pinto LH, Lamb RA (1997) The active oligomeric state of the minimalistic influenza virus M2 ion channel is a tetramer. Proc Natl Acad Sci USA 94:5000–5005

Schaefer J, Stejskal EO, Buchdahl R (1977) Magic-angle C-13 NMR analysis of motion in solid glassy polymers. Macromolecules 10:384–405

Schaefer J, Mckay RA, Stejskal EO (1983) Dipolar rotational spin-echo 13C NMR of polymers. J Magn Reson 52:123–129

Schaefer J, Stejskal EO, Mckay RA (1984) Phenylalanine ring dynamics by solid-state 13C NMR. J Magn Reson 57:85–92

Schaefer D, Spiess HW, Suter UW, Fleming WW (1990) 2D solid-state NMR studies of ultraslow chain motion: glass transition in aPP versus helical jumps in iPP. Macromolecules 23:3431–3439

Schmidt C, Blumich B, Spiess HW (1988) Deuteron two-dimensional exchange NMR in solids. J Magn Reson 79:269–290

Schmidt-Rohr K, Clauss J, Spiess HW (1992) Correlation of structure, mobility, and morphological information in heterogeneous polymer materials by two-dimensional wideline-separation NMR spectroscopy. Macromolecules 25:3273–3277

Schnell JR, Chou JJ (2008) Structure and mechanism of the M2 proton channel of influenza A virus. Nature 451:591–595

Shaw WJ, Long JR, Campbell AA, Stayton PS, Drobny GP (2000) A solid state NMR study of dynamics in a hydrated salivary peptide adsorbed to hydroxyapatite. J Am Chem Soc 122:7118–7119

Smith RL, Oldfield E (1984) Dynamic structure of membranes by deuterium NMR. Science 225:280–288

Stouffer AL, Acharya R, Salom D, Levine AS, Di Costanzo L, Soto CS, Tereshko V, Nanda V, Stayrook S, DeGrado WF (2008) Structural basis for the function and inhibition of an influenza virus proton channel. Nature 451:596–599

Subczynski WK, Wojas J, Pezeshk V, Pezeshk A (1998) Partitioning and localization of spin-labeled amantadine in lipid bilayers: an EPR study. J Pharm Sci 87:1249–1254

Tian F, Song Z, Cross TA (1998) Orientational constraints derived from hydrated powder samples by two-dimensional PISEMA. J Magn Reson 135:227–231

Traikia M, Warschawski DE, Recouvreur M, Cartaud J, Devaux PF (2000) Formation of unilamellar vesicles by repetitive freeze-thaw cycles: characterization by electron microscopy and P-31-nuclear magnetic resonance. Eur Biophys J 29:184–195

van Rossum BJ, de Groot CP, Ladizhansky V, Vega S, de Groot HJM (2000) A method for measuring heteronuclear (H-1-C-13) distances in high speed MAS NMR. J Am Chem Soc 122: 3465–3472

Wang C, Takeuchi K, Pinto LH, Lamb RA (1993) Ion channel activity of influenza A virus M2 protein: characterization of the amantadine block. J Virol 67:5585–5594

Wang J, Schnell JR, Chou JJ (2004) Amantadine partition and localization in phospholipid membrane: a solution NMR study. Biochem Biophys Res Commun 324:212–217

Wang J, Cady SD, Balannik V, Pinto LH, DeGrado WF, Hong M (2009) Discovery of spiro-piperidine inhibitors and their modulation of the dynamics of the M2 proton channel from influenza A virus. J Am Chem Soc 131:8066–8076

Williams JC, McDermott AE (1995) Dynamics of the flexible loop of triosephosphate isomerase: the loop motion is not ligand gated. Biochemistry 34:8309–8319

Yamaguchi S, Huster D, Waring A, Lehrer RI, Tack BF, Kearney W, Hong M (2001) Orientation and dynamics of an antimicrobial peptide in the lipid bilayer by solid-state NMR. Biophys J 81:2203–2214

Yang Z, Liivak O, Seidel A, LaVerde G, Zax DB, Jelinski LW (2000) Supercontraction and backbone dynamics in spider silk: 13C and 2H NMR studies. J Am Chem Soc 122:9019–9025